

# Automated motion correction using parallel-strip registration for wide-field *en face* OCT angiogram

PENGXIAO ZANG,<sup>1,2</sup> GANGJUN LIU,<sup>1</sup> MIAO ZHANG,<sup>1</sup> CHANGLEI DONGYE,<sup>1,3</sup>  
JIE WANG,<sup>1</sup> ALEX D. PECHAUER,<sup>1</sup> THOMAS S. HWANG,<sup>1</sup> DAVID J. WILSON,<sup>1</sup>  
DAVID HUANG,<sup>1</sup> DENGWANG LI,<sup>2,4</sup> AND YALI JIA<sup>1,5</sup>

<sup>1</sup>Casey Eye Institute, Oregon Health & Science University, Portland, OR 97239, USA

<sup>2</sup>Shandong Province Key Laboratory of Medical Physics and Image Processing Technology, Institute of Biomedical, Sciences, School of Physics and Electronics, Shandong Normal University, Jinan, 250014, China

<sup>3</sup>College of Information Science and Engineering, Shandong University of Science and Technology, Qingdao, 266590, China

<sup>4</sup>dengwang.li@139.com

<sup>5</sup>jiaya@ohsu.edu

**Abstract:** We propose an innovative registration method to correct motion artifacts for wide-field optical coherence tomography angiography (OCTA) acquired by ultrahigh-speed swept-source OCT (>200 kHz A-scan rate). Considering that the number of A-scans along the fast axis is much higher than the number of positions along slow axis in the wide-field OCTA scan, a non-orthogonal scheme is introduced. Two *en face* angiograms in the vertical priority (2 y-fast) are divided into microsaccade-free parallel strips. A gross registration based on large vessels and a fine registration based on small vessels are sequentially applied to register parallel strips into a composite image. This technique is extended to automatically montage individual registered, motion-free angiograms into an ultrawide-field view.

©2016 Optical Society of America

**OCIS codes:** (110.4500) Optical coherence tomography; (100.0100) Image processing; (100.2960) Image analysis; (170.4470) Ophthalmology.

## References and links

1. Y. Jia, O. Tan, J. Tokayer, B. Potsaid, Y. Wang, J. J. Liu, M. F. Kraus, H. Subhash, J. G. Fujimoto, J. Hornegger, and D. Huang, "Split-spectrum amplitude-decorrelation angiography with optical coherence tomography," *Opt. Express* **20**(4), 4710–4725 (2012).
2. R. K. Wang, S. L. Jacques, Z. Ma, S. Hurst, S. R. Hanson, and A. Gruber, "Three dimensional optical angiography," *Opt. Express* **15**(7), 4083–4097 (2007).
3. S. Yousefi, Z. Zhi, and R. K. Wang, "Eigendecomposition-based clutter filtering technique for optical micro-angiography," *IEEE Trans. Biomed. Eng.* **58**(8), 2316–2323 (2011).
4. S. Makita, Y. Hong, M. Yamanari, T. Yatagai, and Y. Yasuno, "Optical coherence angiography," *Opt. Express* **14**(17), 7821–7840 (2006).
5. A. Mariampillai, B. A. Standish, E. H. Moriyama, M. Khurana, N. R. Munce, M. K. Leung, J. Jiang, A. Cable, B. C. Wilson, I. A. Vitkin, and V. X. Yang, "Speckle variance detection of microvasculature using swept-source optical coherence tomography," *Opt. Lett.* **33**(13), 1530–1532 (2008).
6. G. Liu, L. Chou, W. Jia, W. Qi, B. Choi, and Z. Chen, "Intensity-based modified Doppler variance algorithm: application to phase instable and phase stable optical coherence tomography systems," *Opt. Express* **19**(12), 11429–11440 (2011).
7. D. Y. Kim, J. Fingler, J. S. Werner, D. M. Schwartz, S. E. Fraser, and R. J. Zawadzki, "In vivo volumetric imaging of human retinal circulation with phase-variance optical coherence tomography," *Biomed. Opt. Express* **2**(6), 1504–1513 (2011).
8. V. X. D. Yang, M. L. Gordon, A. Mok, Y. H. Zhao, Z. P. Chen, R. S. C. Cobbold, B. C. Wilson, and I. A. Vitkin, "Improved phase-resolved optical Doppler tomography using the Kasai velocity estimator and histogram segmentation," *Opt. Commun.* **208**(4–6), 209–214 (2002).
9. B. Park, M. Pierce, B. Cense, and J. de Boer, "Real-time multi-functional optical coherence tomography," *Opt. Express* **11**(7), 782–793 (2003).
10. A. S. Nam, I. Chico-Calero, and B. J. Vakoc, "Complex differential variance algorithm for optical coherence tomography angiography," *Biomed. Opt. Express* **5**(11), 3822–3832 (2014).

11. J. Enfield, E. Jonathan, and M. Leahy, "In vivo imaging of the microcirculation of the volar forearm using correlation mapping optical coherence tomography (cmOCT)," *Biomed. Opt. Express* **2**(5), 1184–1193 (2011).
12. Y. Jia, S. T. Bailey, T. S. Hwang, S. M. McClintic, S. S. Gao, M. E. Pennesi, C. J. Flaxel, A. K. Lauer, D. J. Wilson, J. Hornegger, J. G. Fujimoto, and D. Huang, "Quantitative optical coherence tomography angiography of vascular abnormalities in the living human eye," *Proc. Natl. Acad. Sci. U.S.A.* **112**(18), E2395–E2402 (2015).
13. D. Huang, Y. Jia, and S. S. Gao, "Principles of Optical Coherence Tomography Angiography" in *OCT Angiography Atlas* H. D. Lumbros, B. Rosenfield, P. Chen, C. Rispoli, M. Romano, eds. (Jaypee Brothers Medical Publishers, New Delhi, 2015).
14. S. Martinez-Conde, S. L. Macknik, and D. H. Hubel, "The role of fixational eye movements in visual perception," *Nat. Rev. Neurosci.* **5**(3), 229–240 (2004).
15. R. J. Zawadzki, A. R. Fuller, S. S. Choi, D. F. Wiley, B. Hamann, and J. S. Werner, "Correction of motion artifacts and scanning beam distortions in 3D ophthalmic optical coherence tomography imaging," *Proc. SPIE* **6426**, 642607 (2007).
16. E. A. Swanson, J. A. Izatt, M. R. Hee, D. Huang, C. P. Lin, J. S. Schuman, C. A. Puliafito, and J. G. Fujimoto, "In vivo retinal imaging by optical coherence tomography," *Opt. Lett.* **18**(21), 1864–1866 (1993).
17. B. Braaf, K. V. Vienola, C. K. Sheehy, Q. Yang, K. A. Vermeer, P. Tiruveedhula, D. W. Arathorn, A. Roorda, and J. F. de Boer, "Real-time eye motion correction in phase-resolved OCT angiography with tracking SLO," *Biomed. Opt. Express* **4**(1), 51–65 (2013).
18. I. Gorczynska, J. Migacz, R. J. Zawadzki, N. Sudheendran, Y. F. Jian, P. K. Tiruveedhula, A. Roorda, and J. S. Werner, "En face projection imaging of the human choroidal layers with tracking SLO and swept source OCT angiography methods," *Proc. SPIE* **9541**, 954112 (2015).
19. Q. Zhang, Y. Huang, T. Zhang, S. Kubach, L. An, M. Laron, U. Sharma, and R. K. Wang, "Wide-field imaging of retinal vasculature using optical coherence tomography-based microangiography provided by motion tracking," *J. Biomed. Opt.* **20**(6), 066008 (2015).
20. M. F. Kraus, B. Potsaid, M. A. Mayer, R. Bock, B. Baumann, J. J. Liu, J. Hornegger, and J. G. Fujimoto, "Motion correction in optical coherence tomography volumes on a per A-scan basis using orthogonal scan patterns," *Biomed. Opt. Express* **3**(6), 1182–1199 (2012).
21. H. C. Hendargo, R. Estrada, S. J. Chiu, C. Tomasi, S. Farsiu, and J. A. Izatt, "Automated non-rigid registration and mosaicing for robust imaging of distinct retinal capillary beds using speckle variance optical coherence tomography," *Biomed. Opt. Express* **4**(6), 803–821 (2013).
22. W. Choi, E. M. Moul, N. K. Waheed, M. Adhi, B. Lee, C. D. Lu, T. E. de Carlo, V. Jayaraman, P. J. Rosenfeld, J. S. Duker, and J. G. Fujimoto, "Ultrahigh-Speed, Swept-Source Optical Coherence Tomography Angiography in Nonexudative Age-Related Macular Degeneration with Geographic Atrophy," *Ophthalmology* **122**(12), 2532–2544 (2015).
23. Laser Institute of America, "*American National Standard for the Safe Use of Lasers*," LIA (Amst.) (2014).
24. M. Zhang, J. Wang, A. D. Pechauer, T. S. Hwang, S. S. Gao, L. Liu, L. Liu, S. T. Bailey, D. J. Wilson, D. Huang, and Y. Jia, "Advanced image processing for optical coherence tomographic angiography of macular diseases," *Biomed. Opt. Express* **6**(12), 4661–4675 (2015).
25. R. Estrada, C. Tomasi, M. T. Cabrera, D. K. Wallace, S. F. Freedman, and S. Farsiu, "Enhanced video indirect ophthalmoscopy (VIO) via robust mosaicing," *Biomed. Opt. Express* **2**(10), 2871–2887 (2011).
26. A. F. Frangi, W. J. Niessen, K. L. Vincken, and M. A. Viergever, "Multiscale vessel enhancement filtering," in *Medical Image Computing and Computer Assisted Intervention-MICCAI* (Springer, 1998), pp. 130–137.
27. D. Rueckert, L. I. Sonoda, C. Hayes, D. L. Hill, M. O. Leach, and D. J. Hawkes, "Nonrigid registration using free-form deformations: application to breast MR images," *IEEE Trans. Med. Imaging* **18**(8), 712–721 (1999).
28. S. Lee, G. Wolberg, and S. Y. Shin, "Scattered data interpolation with multilevel B-splines," *IEEE Trans. Vis. Comput. Graph.* **3**(3), 228–244 (1997).
29. G. Wahba, *Spline models for observational data* (SIAM, 1990).
30. E. Peli, "Contrast in complex images," *J. Opt. Soc. Am. A* **7**(10), 2032–2040 (1990).

## 1. Introduction

Optical coherence tomography angiography (OCTA) uses blood flow induced signal variation as an intrinsic contrast mechanism to differentiate vasculature from static tissues [1–11]. OCTA requires repeated B-scans (MB-scan) at one position in order to assess the variation in OCT signal, or decorrelation, of each pixel. Pixels corresponding to vasculature show fluctuations in the OCT signal due to flowing blood cells while pixels of static tissue show little change. Multiple MB-scans are taken in the slow transverse direction to achieve a volumetric OCTA to represent the vasculature. OCTA images can be presented *en face* to replicate the view of traditional dye-based angiography [12,13].

A single OCTA volumetric scan usually takes 3 to 5 seconds, during which involuntary eye movement can introduce motion artifacts to the OCTA images. There are three common types of involuntary eye motions: tremor, microsaccades, and drift [14]. Small motions such as eye drift, tremor, or mechanical instabilities of the OCT apparatus can shift the intensity

distribution within MB-scans at each position. This type of motion results in increased decorrelation signal in static tissue. These mild line artifacts can be suppressed by subtraction of bulk motion signal and by pre-registration of MB-scans [15,16] prior to OCTA computation. Large and rapid motions of the eye such as microsaccades introduce motion artifacts that are clearly visible on *en face* OCTA projections as horizontal or vertical white lines. These large motions artifacts saturates the decorrelation scale and overwhelm flow signal and therefore cannot be corrected by subtraction or registration – these B-frames must be removed. This introduces loss of lines in the *en face* OCTA images that disrupt the continuity of vascular networks. These lines must be replaced with rescanning or by combining redundant data from multiple scans.

Retinal tracking with scanning laser ophthalmoscope (SLO) is one strategy for detecting microsaccadic motion, pausing the OCTA scanning, and then resuming the scan at the proper location [17–19]. However, eye tracking adds complexity and cost to an OCT system, and the slow frame rate of SLO imaging compared with OCT B-frame rate introduces inefficiencies. Other methods that do not require additional hardware were also proposed. Kraus, *et al.* developed an orthogonal registration algorithm to remove the motion error from three-dimensional (3D) volumetric OCT scans that combines the information in horizontal priority (x-fast) and vertical priority (y-fast) volumetric raster scans [20]. This algorithm was adopted in the Avanti OCT system (Optovue, Inc. Fremont, CA) to register OCTA 3D data by detecting the displacements based solely on 3D structural OCT. The computation of this method is very complex because it is performed in 3D. To avoid this complexity, Hendargo *et al.* presented an automatic non-rigid registration method by use of 2 x-fast and 2 y-fast *en face* retinal angiograms [21]. This 2D method is simple and has been successfully demonstrated on  $2.5 \times 2.5$  mm OCTA scan.

While the orthogonal registration methods are effective in minimizing motion artifacts on the current generation machines running 70-100 kHz, the requirement for equal sampling density in both transverse dimensions (x and y) is not ideal for faster machines with speeds above 200 kHz. Considering the optimal time delay between B-frames is around 3-5 ms for OCTA of capillary blood flow [22], the number of A-lines within each B-frame would be higher (600-1000 or higher) than the number of B-frames (<600) that could be accommodated by a comfortable scan time of less than 4 seconds. Therefore, a non-orthogonal scanning and registration scheme would be more efficient.

We have developed a simple and effective strategy to remove motion artifacts using parallel-strip registration and merge two *en face* angiograms in the same transverse priority. A gross registration based on large vessels is used to correct transverse motion, and a fine registration based on small vessels is used to correct discrepancies between two angiograms caused by drift and image warping. The same registration algorithms will be utilized to montage multiple *en face* angiograms into an ultrawide-field view.

## 2. Method

### 2.1 Study population

This study was conducted at the Casey Eye Institute at the Oregon Health & Science University. The study adhered to the tenets of the Declaration of Helsinki and was approved by the Institutional Review Board. Five healthy participants (age,  $30 \pm 5$  years) and two participants with proliferative diabetic retinopathy (PDR) (age, 32 and 67 years) were recruited to the study.

### 2.2 Image acquisition

A prototype OCT system with an axial scan speed of 200 kHz using a swept-source cavity laser (Axsun Technologies Inc., Billerica, MA) operating at a center wavelength of 1045 nm with a tuning range of 100 nm was used. A dual-balanced detector (PDB471C, Thorlabs Inc)

converted the optical signal to electrical signal, and a high speed digitizer (ATS 9360, Alazar Technologies Inc., Pointe-Claire, QC) acquired the electrical signal. A resolution of  $7.5\ \mu\text{m}$  axially and  $12\ \mu\text{m}$  laterally with an imaging depth of  $7\ \text{mm}$  was achieved. The light power exposure at the cornea was  $1.4\ \text{mW}$ , which is within the American National Standards Institute safety limit [23].

Two  $6 \times 10 \times 7\ (\text{x} \times \text{y} \times \text{z})\ \text{mm}$  volumetric y-fast scans were captured at the same region of posterior pole of each eye. Five different regions were scanned on each eye. In each volumetric scan, the beam was scanned  $10\ \text{mm}$  vertically to form a B-frame. Each B-frame consisted of 850 axial lines. At each position, 2 consecutive B-frames (MB-scan) were captured in order to detect motion induced signal variation. The MB-scan is then shifted slightly to a new position along the slow (horizontal) axis. A total 400 slow-axis locations were sampled to form a 3D OCTA volume. This yielded a lateral sampling density of  $11.8\ \mu\text{m}$  along the fast transverse scan axis and  $15.0\ \mu\text{m}$  in the slow axis. One volumetric scan was acquired in approximately 4 seconds.

The split-spectrum amplitude-decorrelation angiography (SSADA) algorithm was used to detect blood flow-induced amplitude change between two consecutive B-frames of the same location [1]. The volume data was segmented along the inner limiting membrane (ILM) and outer plexiform layer (OPL) [24]. The *en face* projection of structural OCT and OCTA was produced by using the mean OCT reflectance value and maximum decorrelation value, respectively, along the axial direction within a slab between the ILM and OPL [1,24] (Fig. 1).

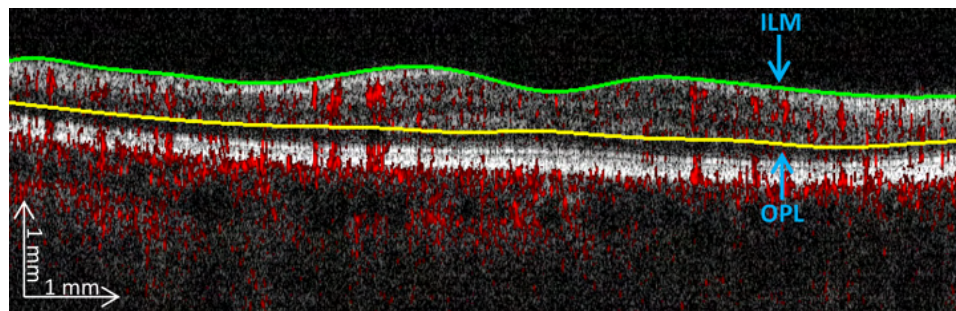


Fig. 1. Segmentation of the inner limiting membrane (ILM, green line) and outer plexiform layer (OPL, yellow line) on one y-fast B-frame from a healthy data set. *En face* images were generated from the mean value of the region between the ILM and OPL. Decorrelation signal is shown in red.

### 2.3 Parallel-strip registration scheme

Two types of motion artifacts affect *en face* OCTA: one that can be corrected by global translation (such as translation, rotation, and focusing differences) of one or more successive B-frames, and another that can be corrected only by local non-rigid deformation within a certain region. To register two scans within the same transverse priority, we divided each *en face* angiogram into parallel microsaccade-free strips. First, the similarity registration based on large vessels was performed to correct large transverse motion. This will be referred to as “gross registration.” Next, the non-rigid deformation based on small vessels (capillaries) is applied to correct small distortion. This is termed “fine registration”. Figure 2 summarizes our algorithm.



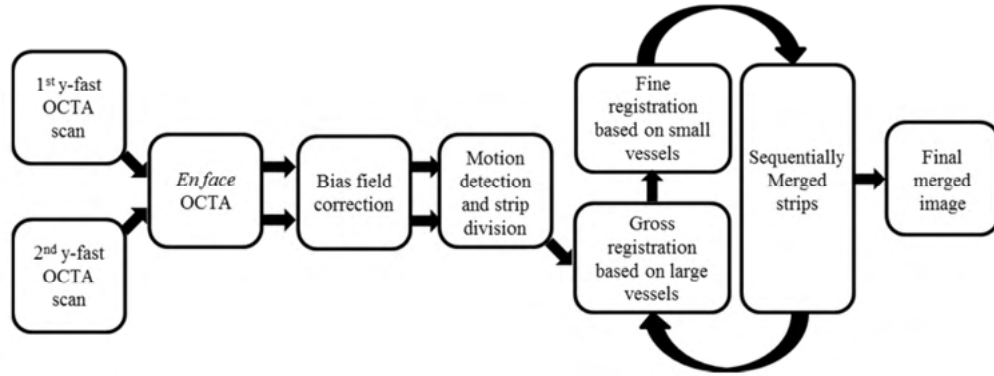


Fig. 2. The flow chart of the automated motion correction algorithm.

### 2.3.1 Bias field correction

The OCT reflectance signal is relatively low in regions where the retina is out of focus (Fig. 3(A) lower-right corner). The decorrelation signal ( $D$ ), which reflects the change of OCT reflectance signal ( $S$ ) within the time between consecutive B-scans, is also reduced in those regions. To correct this dependence, an illumination bias field (Fig. 3(B)) was created by applying a  $X \times Y$  pixel Gaussian filter with 100 pixel standard deviation to the *en face* reflectance image of retina (Fig. 3(A)). The corresponding *en face* angiogram (Fig. 3(C)) was then corrected (Fig. 3(D)) using the bias field.

$$D'(x, y) = D(x, y) * \frac{\text{Mean}(G(S))}{G(S(x, y))} \quad (x = 1, 2, 3, \dots, X; y = 1, 2, 3, \dots, Y) \quad (1)$$

where  $X \times Y$  is the size of the *en face* angiogram,  $\text{Mean}(G(S))$  is the mean value of the bias field,  $D(x, y)$  is the *en face* angiogram and  $G(S(x, y))$  is the bias field by filtering *en face* reflectance image.

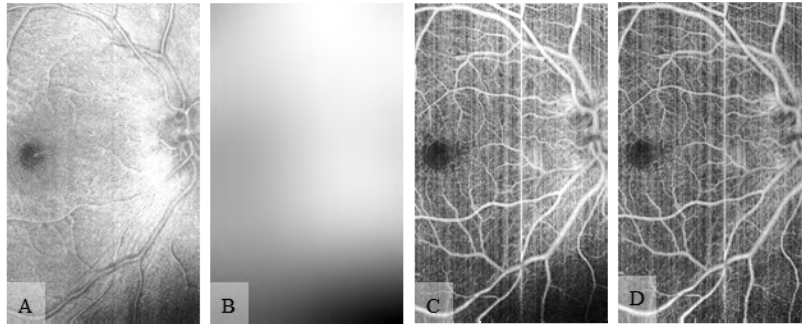


Fig. 3. (A) *En face* mean projection of OCT reflectance. (B) The bias field by Gaussian filtering of (A). (C) Original *en face* angiogram. (D) The *en face* angiogram after bias field correction.

### 2.3.2 Motion detection and strip division

An example of large eye movements manifesting as white lines in OCTA is shown in Fig. 4(B). The decorrelation signals of these lines are generally saturated and do not contain useful blood flow information. Also, the scanned regions on either side of the motion artifact region are usually misaligned. We detected and removed these large motion artifacts as lines (projected B-frames) with mean decorrelation value larger than 1.5 times the mean decorrelation value of the entire *en face* image (Fig. 4(C)).

Small eye movements such as tremor cause incompletely saturated decorrelation variation among B-frames (Fig. 4(C)). To correct this, the decorrelation values in each line are adjusted so that their mean values remain stable (Fig. 5). Next, local histogram equalization with  $5 \times 5$  pixel grid was applied to the whole *en face* image to boost the contrast of capillary vascular network. Gabor filter was applied to enhance the connectivity and facticity of the vasculature (Fig. 4(D)) [25]. The *en face* image was divided into microsaccade-free strips at the detected motion lines (Fig. 4(D)).

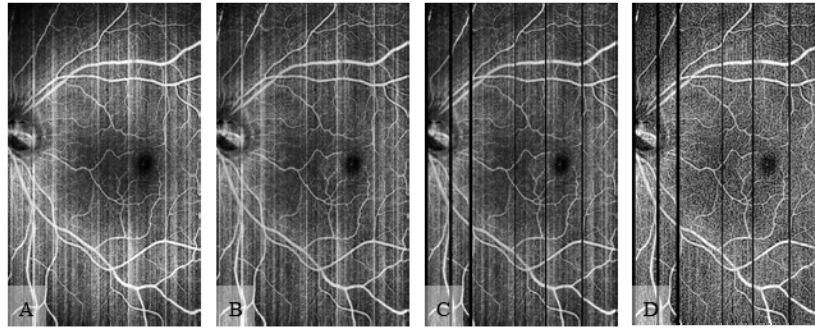


Fig. 4. Motion detection and strip division process of an *en face* OCTA. (A) Original *en face* OCTA. (B) *En face* OCTA after bias field correction. (C) *En face* OCTA after the removal of large eye movements. (D) *En face* OCTA enhanced by the local histogram equalization and Gabor filter. Six microsaccade-free strips were formed for subsequent registration steps.

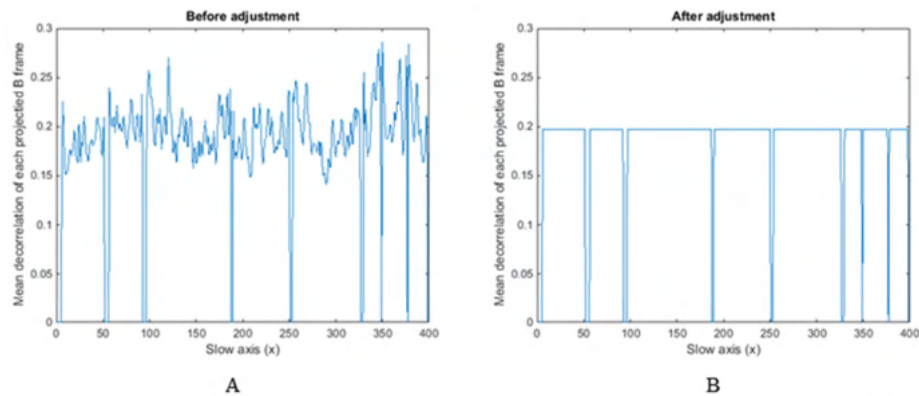


Fig. 5. The plot of mean decorrelation values of projected B-frames on OCTA before (A) and after (B) adjustment. The lines with large eye movements have been removed showing decorrelation values of zero.

### 2.3.3 Gross registration based on large vessels

After the microsaccade-free parallel strips were obtained, a gross registration of *en face* OCTA was performed based on large vessels to correct the malposition among strips. Large vessels were recognized as pixels with a decorrelation value greater than 1.3 times the mean value of the corresponding strip (colored in yellow in Fig. 6(A) and 6(B)). A similarity registration was used to account for translation, rotation, and focusing differences between *en face* strips. The registration process utilized a gradient descent to search for a similarity transformation that minimizes the squared difference of the large vessels of two zero-padded strips.

Specifically, all strips were zero padded to 100 pixels wider and higher than the original *en face* image. Then, any two strips (one from each volumetric scan) containing the largest overlap were considered as the reference strip and moving strip. Here, large vessels are

termed reference large vessel  $L_r(x, y)$  and moving large vessel  $L_m(x, y)$ . The goal is to then find a transformation

$$T_l(x, y, t) = \begin{pmatrix} t_1 & t_2 \\ t_3 & t_4 \end{pmatrix} \begin{pmatrix} x \\ y \end{pmatrix} + \begin{pmatrix} t_5 \\ t_6 \end{pmatrix} \quad (2)$$

of the moving strip that minimizes the squared difference of the reference large vessel and transformed moving large vessel

$$C_l(t) = \sum_{x,y} [L_r(x, y) - L_m(T_l(x, y, t))]^2 \quad (3)$$

where  $(x, y)$  is the pixel coordinate and  $t$  is a vector of transformation parameters. This minimization can be solved iteratively by

$$\begin{aligned} t^{(k+1)} &= t^{(k)} + \alpha d^{(k)} \\ d^{(k)} &= -\frac{\partial C_l^{(k)}}{\partial t} \end{aligned} \quad (4)$$

where  $\alpha$  is the iterative step size, and  $d^{(k)}$  is the gradient descent. An example of the gross registration (Fig. 6(C)) between reference strip (Fig. 6(A)) and transformed moving strip (Fig. 6(B)) is shown in Fig. 6. The gross registration is followed by the fine registration described below.

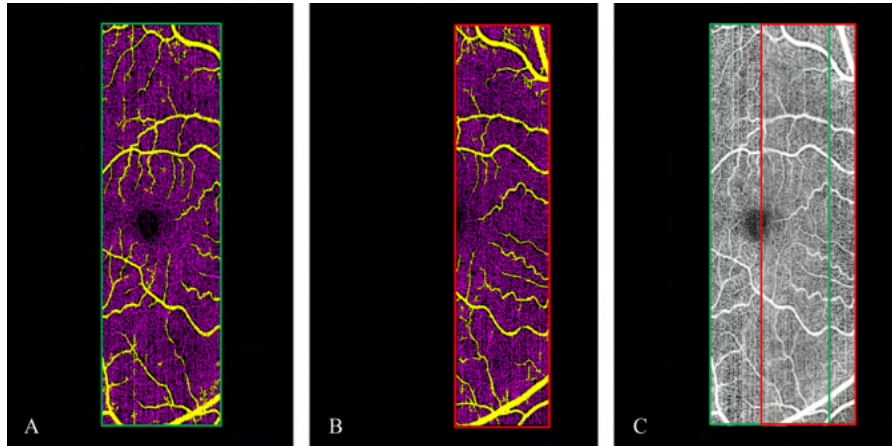


Fig. 6. Example of the gross registration of two microscade-free parallel strips based on large vessels. (A) Reference strip in a zero-padded matrix. (B) Moving strip in a zero-padded matrix. The large vessels are shown in yellow and small vessels are shown in purple. (C) Newly registered strip containing the reference strip (outlined in green) and transformed moving strip (outlined in red).

#### 2.3.4 Fine registration based on small vessels

Slow eye motions within strips, such as those induced by eye drift, cause small scale distortions. We corrected this by aligning the small vessels with a deformable registration of the overlapped area. A multiscale vessel enhancement filter was first applied to enhance the capillary network [26]. Next, pixels that were not previously identified as large vessels, but have decorrelation values greater than 0.6 times the mean value of the entire corresponding strip were defined as small vessels ( $S_r$  and  $S_m$  in reference and moving strips, respectively). Then the fine registration was performed based on the B-spline Free-form deformation (FFD) algorithm [27,28].

The size of the mesh grid was  $n_x \times n_y$  and the control points  $\phi_{i,j}$  were defined as the vertex of each grid. The local deformable field function can be written as:

$$T_s(x, y) = \sum_{p=0}^3 \sum_{q=0}^3 B_p(u) B_q(v) \phi_{i+p, j+q} \quad (5)$$

where  $i = \lfloor x/n_x \rfloor - 1$ ,  $j = \lfloor y/n_y \rfloor - 1$ ,  $u = x/n_x - \lfloor x/n_x \rfloor$ ,  $v = y/n_y - \lfloor y/n_y \rfloor$  ( $\lfloor \cdot \rfloor$  means round down) and  $B_p$ ,  $B_q$  represents the  $p$  or  $q$ -th basis function of the B-spline.

$$\begin{aligned} B_0(u) &= (1-u)^3 / 6 \\ B_1(u) &= (3u^3 - 6u^2 + 4)^3 / 6 \\ B_2(u) &= (-3u^3 + 3u^2 + 3u + 1)^3 / 6 \\ B_3(u) &= u^3 / 6 \end{aligned} \quad (6)$$

The B-splines are locally controlled, so each control point just affects limited points in the neighborhood. Each pixel was calculated according the transformed control points. The  $T_s(x, y)$  was found by a gradient descent method with two weighting cost functions  $C_{smooth}$  and  $C_{similarity}$  [27,29].

$$C_{smooth} = \frac{1}{A_o} \iint_{(x,y) \in A_o} \left[ \left( \frac{\partial^2 T_s}{\partial x^2} \right)^2 + \left( \frac{\partial^2 T_s}{\partial y^2} \right)^2 + \left( \frac{\partial^2 T_s}{\partial xy} \right)^2 \right] dx dy \quad (7)$$

$$C_{similarity} = \frac{1}{A_o} \iint_{(x,y) \in A_o} (S_r - S_m(T_s[T_i(x, y)]))^2 dx dy \quad (8)$$

where  $A_o$  is the area of overlap. Considering the large vessels carries much larger flow than small vessels, their costs are handled separately:

$$C_{fine} = \alpha \cdot (\lambda \cdot CL_{smooth} + CL_{similarity}) + \lambda \cdot CS_{smooth} + CS_{similarity} \quad (9)$$

where  $CL$  and  $CS$  are the cost function for large vessels and small vessels, respectively.  $\lambda = 0.01$  was chosen based on the magnitude of  $C_{smooth}$  and  $C_{similarity}$ , and  $\alpha$  was the weighting value between large vessels and small vessels. In this study,  $\alpha = 9$  was chosen based on a test on pilot data sets. The comparison of registration results with different  $\alpha$  are shown in Fig. 7.

After the optimal transformation was found by a simple iterative gradient descent technique, the overlapped region of grossly registered moving strip  $M(x, y)$  was transformed by the deformable field just obtained.

$$M'(x', y') = M(T_s(x, y)) \quad (10)$$

The completeness, veracity, and distinguishing degree of vasculature in the overlapped region was improved in the final merged image by registering the reference region  $R(x, y)$  and the transformed region  $M'(x', y')$  together. An example comparison of merged OCTA images with and without fine registration are shown in Fig. 8.





Fig. 7. The comparison of merged images registered using different weighting values ( $\alpha$ ) between large and small vessels. The region with size of  $6 \times 5$  mm was selected in this figure. (A) when  $\alpha = 2$ , the merged image shows incorrectly registered vasculatures indicated by yellow boxes. (B) when  $\alpha = 3$ , the merged image is improved, but a double vessel still remains, outlined in the red box. (C) when  $\alpha = 9$ , the registration is optimized and merged image shows the best quality.

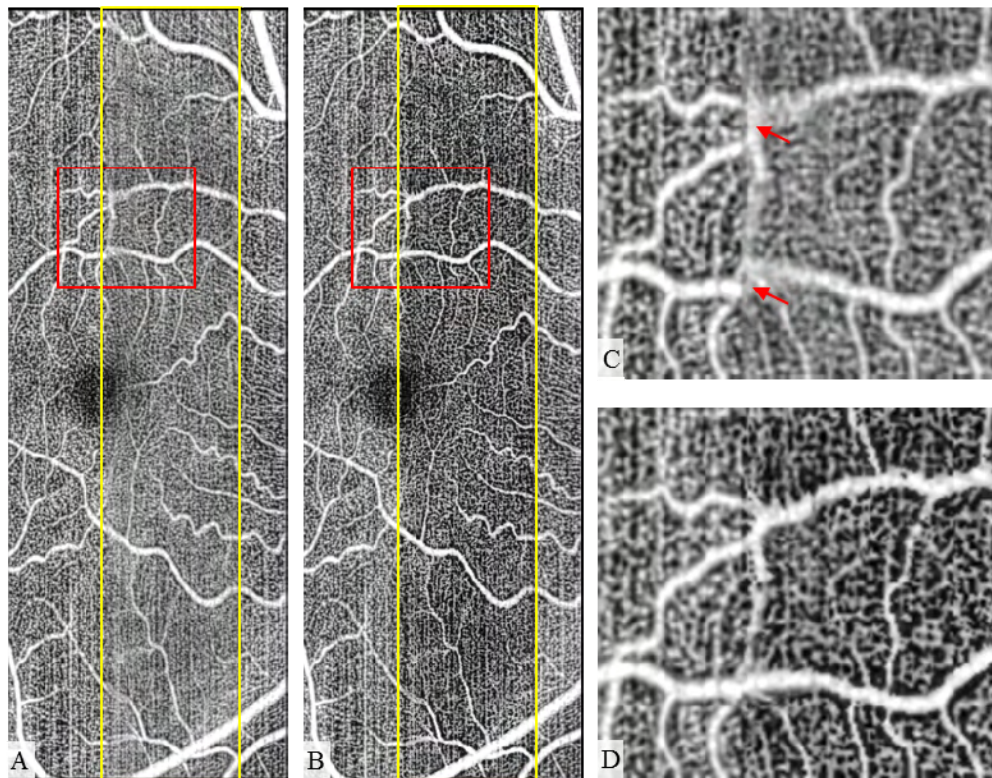


Fig. 8. Comparison of region (outlined in yellow) merged after (A) gross registration and (B) fine registration of two strips. The enlarged regions (outlined in red) in (A) and (B) are shown in (C) and (D), respectively. In (C), the large vessels merged after gross registration are not well connected to the single strip region (pointed by red arrows), and the small vessels are less clear than that of single strip. In (D), the large vessels merged after fine registration are continuous with the single strip and the small vessels are more clear than that of single strip.

The merged strip after both gross and fine registration process is considered as the new reference strip. Next, a new moving strip containing the largest overlap with the new reference strip is registered. This process repeats until all strips are registered and merged into one comprehensive *en face* OCTA image.

### 2.4 Montage of adjacent widefield images

The method described above can be applied for the automatic montage of widefield OCTA *en face* images acquired at a known region of the eye and contain an overlap of consistent vascular patterns. In this study, a  $23 \times 10$  mm montage was generated using five OCTA scans that each covered an area of  $6 \times 10$  mm. The five scans were sequentially acquired from peripapillary to temporal regions by changing the fixation target. This allowed for adjacent scans to have small areas of overlap, around  $1.5 \times 10$  mm. Each scan was considered to be a separate strip during the registration procedure.

### 3. Results

The automated parallel-strip registration between two strips took on average 11.8 seconds and within that time, the preprocessing step (Methods 2.3.1 and 2.3.2) took about 5.9 seconds. The test was performed on a workstation with *Inter(R) Xeon(R) CPU E3-1226 v3 @ 3.30GHz* and *16.0 GB RAM* using MATLAB 2014b (*Mathworks, Natick, MA*).

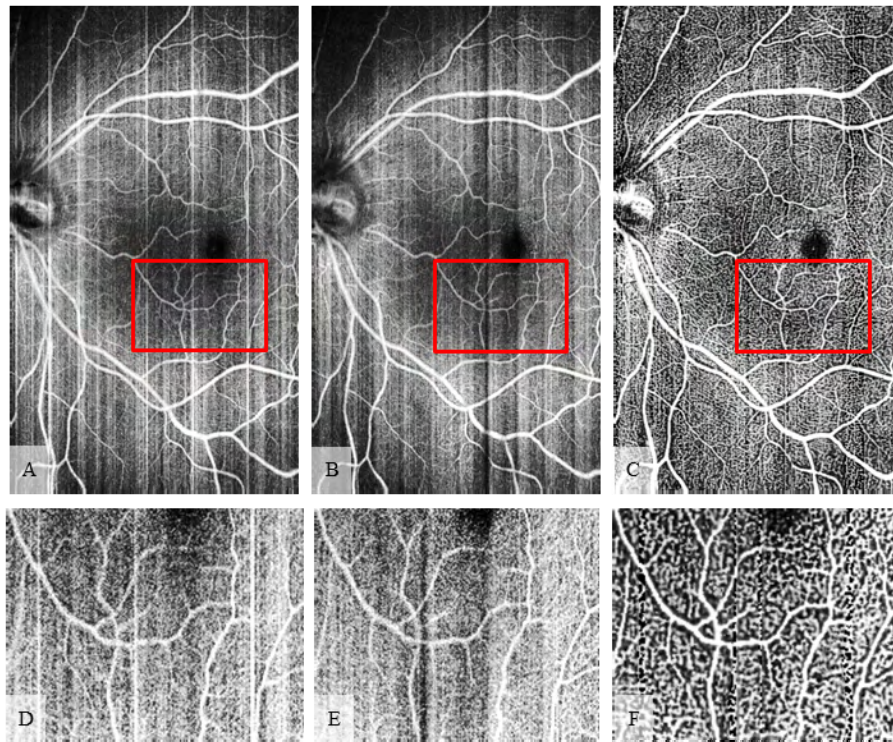


Fig. 9. Removal of artifacts using parallel-strip registration of two y-fast *en face* OCTA images ( $6 \times 10$ mm) of a healthy retina. (A) 1st y-fast *en face* OCTA. (B) 2nd y-fast *en face* OCTA. (C) merged image after using proposed parallel-strip registration of Panels A and B. (D), (E) and (F) are the enlarged region (outlined in red) of the same region of Panels A, B and C.

Figure 9 shows *en face* OCTA of a healthy retina before and after applying parallel-strip registration method to y-fast scans (Fig. 9(A)-9(B), 9(D)-9(E)). Large transverse motion artifacts and incoherence of vasculature were corrected in the merged image (Fig. 9(C), 9(F)). On Fig. 9(A) and 9(B), it can be observed that the flow signal at the lower and upper left corners of *en face* image is poor, resulting in the capillaries having low contrast. These defects have been corrected (Fig. 9(C)) using the proposed method. Retinal capillary networks which were affected by motion artifacts in the original y-fast *en face* OCTAs can be easily identified in the merged image (Fig. 9(C) and 9(F)). Also, the background has been suppressed while flow signals have been enhanced.



By visual inspection, motion artifacts were reduced in all merged wide-field *en face* angiograms after parallel-strip registration compared to unregistered y-fast scans. To quantitatively evaluate the capability to remove microsaccadic motions, we counted the number of microsaccade motion artifacts (white lines) present in original *en face* y-fast OCTA, and the number of microsaccade motion artifacts corrected by the registration algorithm. We found 100% of large movement artifacts were successfully removed in 50 y-fast scans of normal eyes and 20 y-fast scans of eyes with PDR. When microsaccade motion artifacts are overlapped between the two y-fast scans (Fig. 10(A) and 10(B)), the interpolation process was applied. The motion artifact overlap was filled based on neighboring pixels. Since the number of missing lines is only 1 or 2 in all the scans we processed and interpolation can achieve seamless filling (Fig. 10(C)), it seems the overlap of microsaccade should not be problematic. It should be noted that the residual variation in the vessel brightness between lines is due to the uneven number of original scans merged in the final *en face* OCTA. For example, the lines registered and merged from two scans show more capillary network and the lines composed of only one scan show less capillary network.

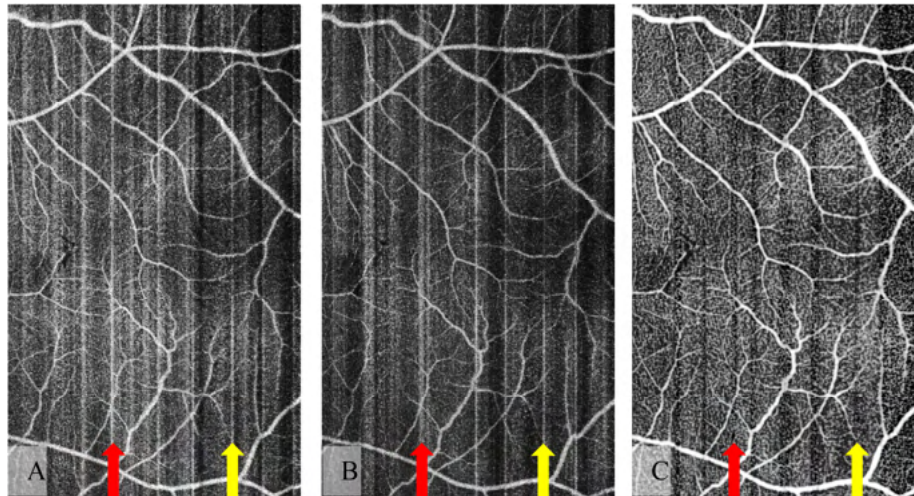


Fig. 10. Interpolation of positions in registered and merged *en face* OCTA image with overlapped microsaccade motion artifacts in original y-fast scans. (A) 1st y-fast *en face* OCTA. (B) 2nd y-fast *en face* OCTA. (C) merged image. The interpolation was performed on the lines with missing flow information due to overlapped microsaccades. The overlapped artifacts and the corresponding regions fixed by interpolation were indicated by red (1st example) and yellow (2nd example) arrows.

To quantitatively evaluate how fine registration improves the image contrast, the root mean square (RMS) contrast [30] was used and is defined as the standard deviation of the decorrelation value Eq. (11).

$$C_{RMS} = \sqrt{\frac{1}{A} \times \sum_{(x,y) \in A} (M(x,y) - \bar{M})^2} \quad (11)$$

where  $A$  is the area of the merged image,  $M(x,y)$  is the decorrelation value of coordinate  $(x,y)$  and  $\bar{M}$  is the mean decorrelation value of the entire merged image. Comparison of the  $C_{RMS}$  before and after fine registration was performed on all  $6 \times 10$  mm *en face* OCTA in this study. The improvement of contrast is shown in Table 1.

Table 1. The Comparison of the RMS Contrast

RMS contrast (mean $\pm$ sd)	Before fine registration	After fine registration	Improvement
---------------------------------	-----------------------------	----------------------------	-------------

Normal	$0.18 \pm 0.03$	$0.25 \pm 0.03$	35.5%
PDR	$0.19 \pm 0.02$	$0.25 \pm 0.04$	31.8%

The eye of PDR is characterized by heterogeneous vasculature with areas of drop out as well as new vessels that are present above the ILM (vitreous slab). Proliferative vasculature in the vitreous slab was registered and merged according to the deformable field obtained from the registration of the retina layer (Fig. 11). After motion removal and registration, the nonperfusion areas are more distinctive and the neovascular network is more continuous, compared to the original non-registered images.

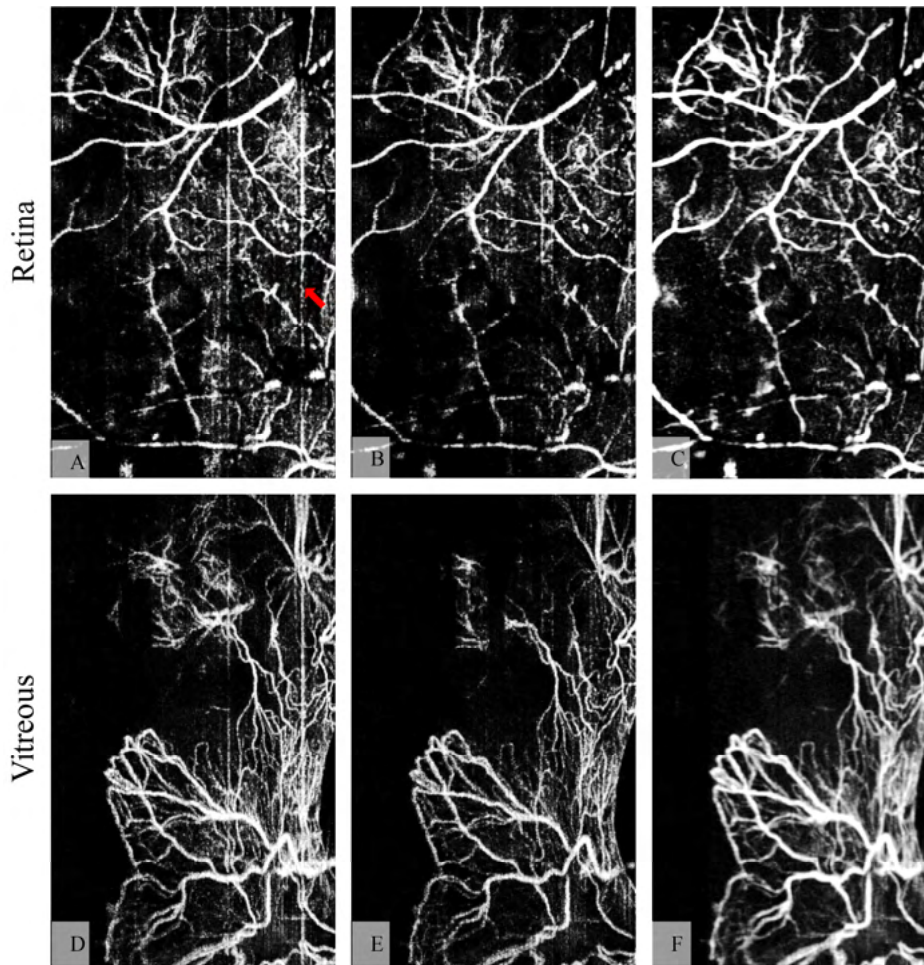


Fig. 11. Registration of two y-fast *en face* OCTA ( $6 \times 10\text{mm}$ ) of an eye with proliferative diabetic retinopathy (PDR). (A) 1st y-fast *en face* OCTA of retina. (B) 2nd y-fast *en face* OCTA of retina. (C) Merged retinal image using proposed parallel-strip registration. (D) 1st y-fast *en face* OCTA of vitreous with retinal neovascularization (RNV). (E) 2nd y-fast *en face* OCTA of vitreous with RNV. (F) Merged vitreous image by applying deformable field obtained from the retinal slab. Red arrow indicates a vertical motion artifact crossing through a nonperfusion region.

We also demonstrated the ability to perform automated ultrawide-field montage using the same registration scheme. Figure 12 shows  $25 \times 10\text{mm}$  ultrawide-field OCTA of retinal vasculature in a normal subject. It can be observed that the integrity of retinal vasculature throughout the entire posterior pole of the eye was greatly recovered by registration process. The whole angiogram is fairly homogenous.



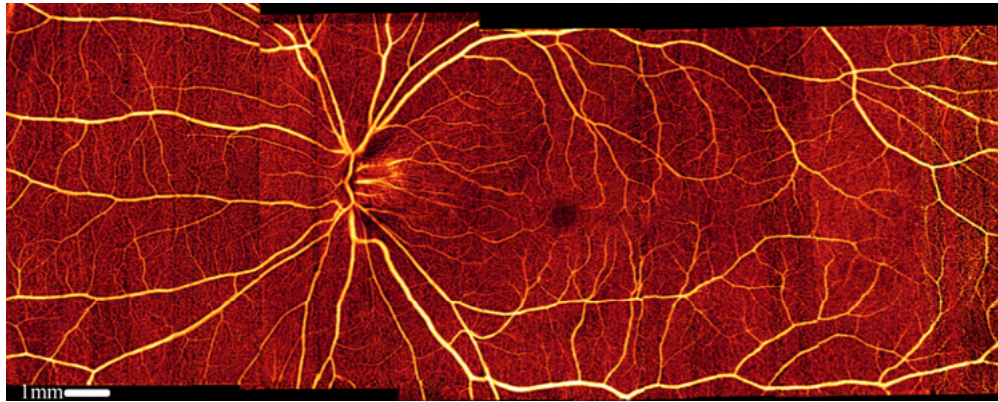


Fig. 12. Automated ultrawide-field montage ( $25 \times 10\text{mm}$ ) by registering and merging five motion-corrected wide-field image ( $6 \times 10\text{mm}$ ).

#### 4. Discussion

We have developed a parallel-strip registration method to remove motion artifacts on a ultrahigh-speed OCTA system. This method is well suited for the rectangular scan pattern of ultrahigh-speed OCT, and can help in generating ultrawide-field OCTA images of retinal vasculature.

In the motion detection step, a threshold of 1.5 times the mean decorrelation value of whole *en face* image was used to detect the microsaccadic motion artifacts in the corresponding B-frame. This threshold was chosen based on the pilot data sets acquired from healthy subjects. It works well in almost all data set in this study except when a large portion of B-frame contained a large vessel parallel to the B-frame. This will lead to a false positive motion detection. However, this situation is uncommon since vessels typically possess some level of curvature.

In the PDR patient scans, the vitreous layer with retinal neovascularization was registered and merged based on the deformable field obtained from the retina slab. Here we ignored the motion difference between vitreous and retina because of the high speed A-scan rate ( $5\mu\text{s}/\text{A-line}$ ). As we expected, slight registration artifacts are not visible in the images of vitreous slab.

In this study, the commonly used pre-registration between two repeated B-frames wasn't applied, but an alternative method, i.e. brightness adjustment between fast scans was chosen to eliminate the artifacts caused by small motions. We have several reasons for this decision. First, SSADA algorithm splits the spectrum into several spectral channels to enhance the flow detection and simultaneously reduce the sensitivity of eye motion along laser beam direction (z-axis) [1]. Second, the pre-registration between B-frames is very time-consuming and only corrects the motions at y and z axes in our case, but not the direction perpendicular to B-frames (x-axis). Whereas, the equalization of decorrelation value between lines (projected B-frames) can minimize the artifacts caused by motions, regardless of their directions. Shown by our results, this simple step used in our algorithm is very effective.

A limitation of this method is that only the information from one scan can be used at lines with microsaccade motion artifacts in the merged image, which generates less dense vessel density than that of lines with information from two scans. To overcome this variation, registering three repeated scans and merging two registered scans can be considered in practice.

Another limitation of this study is that the lateral sampling space used in this scan protocol is relatively low. Scanning a smaller dimension on both fast and slow axes would allow for a larger A-line density and subsequent enhanced angiogram contrast, which will facilitate the

application of registration algorithm. Further study is needed to optimize the relationship between the registration performance, the scan size, and the sampling density.

## 5. Conclusion

In summary, we proposed an automated motion correction algorithm using parallel-strip registration to remove motion artifacts and improve image quality by merging two *en face* angiograms scanned by a ultrahigh speed, swept source OCT. We corrected the motion artifacts using gross registration based on the large retinal vessels and fine registration based on the small retinal vessels using free-form deformation. We tested our algorithm on healthy control and PDR patients. We also demonstrated our method can be used for the automated ultrawide-field montage. The study indicates this method may help to improve the diagnostic accuracy by improving integrity of retinal vasculature.

## Acknowledgments

This work was supported by NIH grants DP3 DK104397, R01 EY024544, R01 EY023285, P30 EY010572, Oregon Health & Science University (OHSU) foundation, NSFC (Grant No. 61471226), Natural Science Foundation for Distinguished Young Scholars of Shandong Province (Grant No. JQ201516) and unrestricted grant from Research to Prevent Blindness. Financial interests: Financial interests: OHSU, David Huang and Yali Jia have a significant financial interest in Optovue. David Huang also has a financial interest in Carl Zeiss Meditec. These potential conflicts of interest have been reviewed and managed by OHSU.